Multiscale Hybrid Modeling of Film Deposition Within Porous Substrates

M. Gummalla, M. Tsapatsis, and J. J. Watkins
Dept. of Chemical Engineering, University of Massachusetts Amherst, Amherst, MA 01003

D. G. Vlachos
Dept. of Chemical Engineering, and Center for Catalytic Science and Technology, University of Delaware, Newark, DE 19716

A multiscale, hybrid computational framework for the deposition of films within porous substrates, is developed and applied to a prototype deposition reaction in the opposed reactant flow geometry. The developed model captures transport of reactants through the pores, homogeneous reaction of reagents producing an intermediate species, nucleation, and growth of the film as a moving boundary problem. The pore evolution is described using a capillary model. Adaptive mesh refinement is used to resolve length scales varying from nanometers to one millimeter. Nucleation is treated stochastically at the finest level, whereas transport and reaction at coarser levels are treated deterministically. Transport parameters chosen for these simulations correspond to the deposition of Pd films in porous alumina under supercritical CO_2 conditions. The numerical results provide insight into the strategies that could be used to control their thickness, including confining thin films within substrates. For example, it has been found that the location of the deposit within the porous substrate is essentially determined by the relative concentrations of reagents on either side of the porous substrate, and the startup of the process. In addition, it is shown that the interplay of nucleation and growth kinetics determines the morphology and roughness of the deposit at short time scales. © 2004 American Institute of Chemical Engineers *AIChE J,* 50: 684–695, 2004

Keywords: crystal growth, multiscale modeling, materials, nucleation, mathematical modeling

Introduction

Thin films are used in numerous applications that involve optics, catalysts, coatings, microelectronics, sensors, and membrane reactors. Control of film thickness, surface microstructure, and morphology is crucial to meet the requirements of advanced materials. Several techniques have been developed to fabricate thin films under varying environments and operating conditions, such as sputtering, electroless deposition, chemical vapor deposition (CVD), and supercritical fluid deposition (SFD). Manufacturing reproducible, defect-free films with a controlled microstructure at low cost still remains a challenge. To achieve the above goals, a fundamental understanding of the deposition process and optimization of the operating conditions is imperative. Hence, considerable effort has been directed towards the modeling of the CVD process (Lin and Burggraaf, 1991; Ofori and Sotirchos, 1996; Sotirchos and Zarkanitis, 1993; Tsapatsis and Gavalas, 1992, 1997; Xomeritakis and Lin, 1994b). Deposition within a porous media is in many cases desirable in order to enhance adhesion, and also to avoid peel off, and minimize or effectively dissipate stresses to the support, induced, for example, in the case of hydrogen diffusion through a Pd film.

Experimental and numerical studies have been conducted on the deposition of inorganic and organic thin films within porous

Correspondence concerning this article to D. G. Vlachos at vlachos@che.udel.edu.

media by reactants flowing from opposite sides of a porous medium (Tsapatsis and Gavalas, 1992, 1997; Xomeritakis and Lin, 1994a, b, 1998). Theoretical models describing deposition, which account for reaction-transport-pore evolution, are either simple models solved semi-analytically (Xomeritakis and Lin, 1994b), or complex models solved numerically (Ofori and Sotirchos, 1996; Sotirchos and Zarkanitis, 1993; Tsapatsis and Gavalas, 1992, 1997). Lin and coworkers have developed continuum chemical vapor infiltration (CVI) and CVD models using the dusty gas model for describing transport and the quasi-steady-state assumption (Lin and Burggraaf, 1991; Xomeritakis and Lin, 1994b). Tsapatsis and Gavalas assumed a simple transport and random capillary model to numerically investigate deposition of silica and alumina in porous Vycor tubes by hydrolysis of $SiCl_4$, and oxidation of the aluminum precursor (Tsapatsis and Gavalas, 1992), respectively. Decorated lattice models were used to subsequently describe pore connectivity, and thus, identified that the deposited films were relatively thinner, and were produced in less time (Tsapatsis and Gavalas, 1997), compared to that previously reported in Tsapatsis and Gavalas (1992). More recently, it was shown that transients may strongly affect the deposit location under certain conditions, and, therefore, the quasi-steady-state assumption may break down (Gummalla et al., 2002).

Nucleation and growth are important aspects of film deposition. However, in most previous work, nucleation has not been explicitly considered. Conventionally, nucleation is modeled at the continuum level through a Heaviside function, classic nucleation theory, or Cahn-Hilliard based models (Dee, 1986; Girshick et al., 2000; Gummalla et al., 2003; Lebedeva et al., 2004; Samseth et al., 1998) that usually link the nucleation rate to the level of supersaturation. Aside from missing the microscopic physics and stochastic effects, use of the Heaviside function in the models can lead to results that depend on the discretization of the governing equations when nucleation is very fast, and a coarse mesh is used (Gummalla, 2002). Furthermore, growth is itself a moving boundary (Stefan) problem, but diffusion-reaction models have not treated it as such. Nucleation and growth initiate at the nanometer length scale where thermal fluctuations are typically important and evolve to considerably larger length scales. Currently, there are no models that can resolve these issues. Here, a prototype multiscale, hybrid framework for deposition of thin films within porous substrates is developed. The feasibility of the developed framework to model deposition processes is presented, followed by some parametric studies. The proposed model is universally applicable to the deposition of films in porous media; however, in this article the focus is on a specific example of Pd films in alumina, formed by the reaction of H_2 and P (π-2-methylallyl (cyclopentadienyl) palladium (II)) precursor, and we use relevant terminology.

Reaction Mechanism and Rates

A prototype reaction mechanism, consisting of three basic steps, is assumed. The precursors H_2 and P, present in dilute amounts, are assumed to react in the fluid phase, within the pores, producing an intermediate species I, through reaction R1

$$H_2 + P \rightarrow I + \text{Byproducts} \quad \text{(homogeneous reaction)} \quad \text{(R1)}$$

$$2I \rightarrow M + 2L \quad \text{(nucleation)} \quad \text{(R2)}$$

$$I + H_2 \xrightarrow{M} M + L \quad \text{(heterogeneous growth)} \quad (R3)$$

The intermediate is envisaged as a molecule comprised of a metal atom (M), linked with some organic ligands (L). When the concentration of the intermediate is sufficiently high, the probability of the formation of a stable nucleus through reaction R2, is also high. On the basis of analysis of STM studies on metal deposition at low temperatures, it is considered that the dimer is the critical nucleus in this model (Brune, 1998). Finally, each nucleus provides active sites for dissociation of the intermediate species to form metal and organic ligands through reaction R3.

Details of actual kinetics for many systems are not often available. For this reason, prototype, simple powerlaw rate expressions have been used with exponents reflecting the stoichiometry of reaction R1. The rate of reaction R1 is taken as

$$r_1 = K_1 C_{H_2} C_P \tag{1}$$

where K_1 is the volumetric reaction rate constant, and C_i is the molar concentration per unit pore volume of species i ($i = H_2$, P).

For the growth kinetics (reaction R3), the following expression is used for the growth rate

$$r_3 = K_{\text{Het}} C_I C_{H_2}^{0.5} \tag{2}$$

The reaction orders can be obtained in the zero coverage limit of Langmuir-Hinshelwood kinetic regime (half-order kinetics reflects dissociative adsorption of H_2). Other kinetic expressions are straightforward to incorporate in the multiscale framework; however, it is left for future research. Aside from the chemical reactions, transport of the chemical species within the open pores, and within the growing nanocrystalline metal deposit, must be considered.

Governing and Constitutive Equations of Transport

The governing conservation equations for reaction and transport are

$$\frac{\partial\{C_i(\varepsilon + H_i(\varepsilon_o - \varepsilon))\}}{\partial t} = \nabla \cdot (j_i^f + j_i^s) + \sum_{j=1}^{2} v_{ij} \varepsilon r_j + v_{i3} S_\varepsilon r_3$$

$$i = H_2, P, I, \text{ and } j = \text{R1, R2} \tag{3}$$

Here, t is the time, ε is the porosity of the medium (ratio of void volume to total volume), ε_0 is the porosity at time $t = 0$, H_i is the Henry's equilibrium coefficient of species i in the solid medium, r_j is the rate of j^{th} reaction, and v_{ij} is the stoichiometric coefficient of species i in reaction j. The stoichiometric coefficient is assumed to be positive for products, and negative for reactants. In addition, j_i^s and j_i^f are the fluxes of the i^{th} species in the deposit and the fluid phase, respectively.

S_ε is the surface area per unit volume of the substrate. Transport of H_2 occurs through the gas phase, as well as by dissolution and diffusion through the metal. The diffusion of all species through the substrate is neglected due to its low value.

Transport of reactants through the open pores

Multicomponent mass transport in porous media is often modeled using the dusty gas model (DGM), the mean-transport-pore model (MTPM), or the binary friction model (BFM) (Kerkhof, 1996, 2001; Mason and Malinauskas, 1983; Novak et al., 1988). These models were derived from the Stefan-Maxwell's description of multicomponent transport in pores, and Darcy's equation for permeation. Depending on the structure of the porous medium, bulk diffusion, Knudsen diffusion, and/or convection can be relevant. For highly diluted reactant systems at isothermal and isobaric conditions, the DGM model simplifies (Sloot et al., 1992) to the following approximate expression

$$j_i^f = -\frac{D_i \varepsilon}{\tau} \cdot \nabla C_i \tag{4}$$

Here, τ is the tortuosity of the porous medium, and D_i is the average diffusivity of species i. When the pores are sufficiently large, D_i is the ordinary molecular diffusivity. Assuming kinetic theory of ideal gases under supercritical pressures, the mean free path for hydrogen is ~3 nm. Therefore, Knudsen diffusion is considered unimportant in the present calculations because of primary interest in short times.

The molecular diffusion coefficients used in the present simulations are taken from experiments (Fernandes et al., 2001), based on the method of Fuller et al. (1966) with a high-pressure correction obtained from a correlation by Takahashi et al. described in Reid et al. (1987). Theoretical calculations for D_i based on Hongqin and Ruckenstein, (1997), were performed in some cases, and good comparison with the experimental data (Fernandes et al., 2001) was found.

Transport of H_2 through the metal

H_2 and few other gases diffuse through metals (Troiano, 1973; Ward and Dao, 1999). Hydrogen permeation includes external mass transfer, (dissociative) surface adsorption, transition from the surface to the bulk metal, diffusion within the bulk metal, transition from the bulk metal to the surface, and (associative) surface desorption. Transport through the metal could occur along grain boundaries, or through the polycrystalline metal itself. The latter is an order of magnitude slower than the former (Kirchheim et al., 1988).

Assuming thermodynamic equilibrium and Fick's first law, the mass diffusion fluxes through the solid are

$$j^s_{H_2} = -\frac{D_{H_2,M}(\varepsilon_o - \varepsilon)}{\tau} \cdot \nabla(H_{H_2} C_{H_2}), j^s_P = 0, \text{ and } j^s_I = 0 \tag{5}$$

where H is the partition coefficient. For the majority of the simulations and chosen parameters in our studies, this diffusion mechanism does not play a significant role.

Nucleation and Growth

Theoretically, Ratsch et al. (2000) have recently discussed deterministic, random, and probabilistic methods for modeling nucleation. In the deterministic model, a nucleus is seeded at the location where the concentration of the intermediate is above a predetermined value. This is similar to using the conventional Heaviside function (Lebedeva et al., 2004; Samseth et al., 1998) in continuum models. In the random nucleation model, the nucleus emerges at any location at random, independent of the spatial distribution of the intermediate. In the probabilistic nucleation model, the position where the nucleus forms is weighted by the local squared concentration of the intermediate C_I^2. It has been found that the size distribution of the clusters obtained from the probabilistic nucleation model was in excellent agreement with kinetic Monte Carlo simulations, as well as with experimental data.

For irreversible nucleation on a surface lattice with a dimer as the critical nucleus, the rate of nucleation is (Bales and Chrzan, 1994)

$$R_{\text{nuc,het}} = 2D\sigma\langle C^2_{I,\text{ads}}\rangle \tag{6}$$

where D is the adatom diffusion constant on the surface, σ is the adatom capture number, and $\langle C^2_{I,\text{ads}}\rangle$ is the spatial average surface concentration of the adsorbed intermediate.

In the case of homogeneous nucleation, the nucleation rate is proportional to the collision rate of the intermediate species (Hill, 1977), and is given by

$$R_{\text{nuc,hom}} = 2P_c C_I^2 N_A^2 \sigma_I^2 \sqrt{\frac{\pi k_B T}{m}}\, e^{-E_c/\text{RT}} \tag{7}$$

where σ_I is the diameter of the intermediate, k_B is the Boltzmann constant, T is the temperature of the medium, E_c is the activation energy, N_A is the Avogadro number, P_c is the steric factor, and m is the molecular mass of the species.

In the present case, the nucleation is considered as an association of two radicals of the intermediate, with the release of few organic ligands, according to reaction R2. By analogy to the above cases, the nucleation rate of step R2 is written as

$$r_2 = k_{\text{nuc}} C_I^2 \tag{8}$$

where the rate constant k_{nuc} could be strongly dependent on temperature.

Monte Carlo (MC) offers a brute force method to simulate nucleation. An area where kinetic MC has routinely been used is nucleation and growth of thin films (Gilmer, 1980; Lam and Vlachos, 2001). Typical two-dimensional (2-D) MC simulation boxes range from 40 × 40 up to 1,000 × 1,000, which correspond to 16 nm × 16 nm up to 400 nm × 400 nm (assuming a lattice size of 0.4 nm). Furthermore, with a few exceptions (Katsoulakis et al., 2003; Vlachos and Katsoulakis, 2000; Lam et al., 2001; Snyder et al., 2003), MC simulations have been limited to situations where the external field (such as pressure) is uniform, and, as a result, they are carried out under periodic boundary conditions. Numerous practical systems are much larger in size (such as millimeters to many inches), and exhibit gradients across the domain (Raimondeau and Vlachos,

2002). Application of MC methods for such large length and time scales and systems under gradients is impractical. Our system is relatively large (the alumina disk thickness is ~1 mm), and exhibits gradients in concentrations of species due to the countercurrent configuration and the presence of chemical reactions. Therefore, a hybrid method using the Poisson distribution function is employed in which the first three discretization levels are treated deterministically, whereas nucleation at the 4th level is treated stochastically (see below for adaptive mesh methodology). In particular, the probability for nucleation P_o is proportional to the nucleation rate, and is expressed as molecules per second. The probability for a nucleation event in a time t_{nuc} after the creation of a previous nucleus is assumed to be (Toschev et al., 1972)

$$P(t_{\text{nuc}}) = 1 - \exp[-t_{\text{nuc}}P_o] \tag{9}$$

where

$$P_o = r_2 N_A \Delta V_n / 2 \tag{10}$$

Here, ΔV_{n} is the volume available for the molecular collisions within a pore of radius r_o and equal length to the discretization ΔX_n of the appropriate n^{th} mesh level (discussed further in the numerical section). The factor of 2 in Eq. 10 accounts for all possible combinations of the reacting molecules and is a consequence of interaction between averaging and the nonlinear operators (Scappin and Canu, 2001). At every time step, the probability for nucleation is computed at all spatial locations. Similar to Vekilov et al. (1997) $P(t_{\text{nuc}})$ is computed and compared at every time step with a random number between 0 and 1. When the random number is larger than $P(t_{\text{nuc}})$, t_{nuc} is incremented by Δt, whereas, when the random number is less than $P(t_{\text{nuc}})$, a new nucleus is seeded and t_{nuc} is set to zero. Validation of approximating the nucleation through the aforementioned approach has been carried out in a well-mixed batch reactor (analogous to one node) by comparing fully stochastic MC simulations to the hybrid approach proposed here by using Eq. 9, and good agreement was found as shown in Appendix A.

Growth, which occurs on newly born nuclei and already growing clusters, is described as a moving boundary problem. Common techniques to simulate the moving interface of growing materials include the front tracking, the level-set, and phase field models, for example, Bonilla et al. (2001); Gyure et al. (1998); Kyu and Chiu, (2002); Osher and Sethian (1988); Vekilov et al. (1997). The velocity of the moving interface is proportional to the rate of metal production and is

$$V = \frac{r_3}{\Omega} \tag{11}$$

where Ω is the atomic volume of the crystal. The growth at every point depends on the local concentration of the intermediate through the heterogeneous growth rate, given by Eq. 2.

Pore evolution

Continuum and discrete models have been developed to describe porous media (Sahimi et al., 1990). Continuum models include the grain model (Szekely and Evans), or capillary

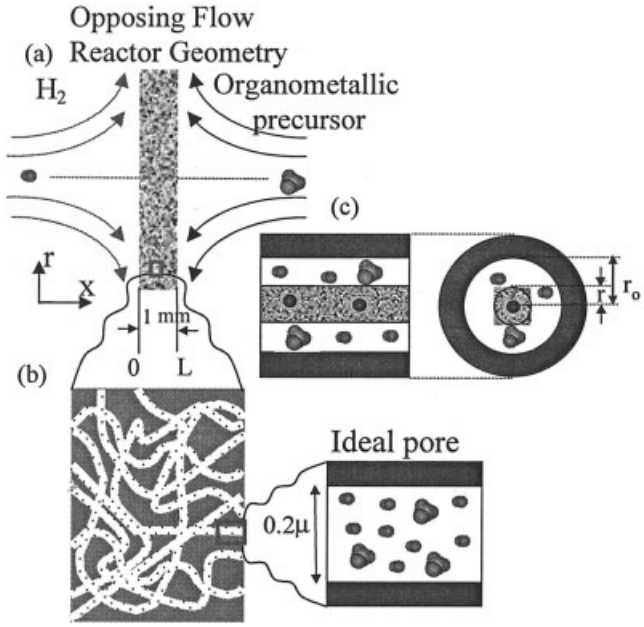

Figure 1. (a) Opposing reactants geometry, (b) porous medium filled with capillaries of uniform radius and an ideal pore, and (c) growth due to nucleation.

models. Among capillary models, the random pore model (Hashimoto and Silveston, 1973), the pore tree model (Simons and Finson, 1979), and the random capillary model (Bhatia and Perlmutter, 1980; Gavalas, 1980) are well known. In the present study, we consider an idealized capillary model, where the porous substrate is treated as a solid matrix filled with open cylindrical tubes of the uniform radius (see Figure 1b). A single pore is depicted in Figure 1c. Depending on the interaction properties of the substrate and depositing material (such as wettability and surface tension), the deposit could grow along the surface of the substrate (heterogeneous nucleation) or in the fluid phase (homogeneous nucleation). Homogeneous nucleation is only considered in the current simulations, as shown in Figure 1c. The surface area per unit volume of the substrate and the porosity can be expressed as functions of the pore radius (Xomeritakis and Lin, 1994b)

$$\frac{dr_\varepsilon}{dt} = V \text{ or } r_\varepsilon = \int_0^t V\text{dt} \tag{12}$$

$$S_\varepsilon = \frac{2\sqrt{\varepsilon_o}\sqrt{\varepsilon}}{r_o} \tag{13}$$

$$\varepsilon = \varepsilon_o \left(\frac{r_\varepsilon}{r_o}\right)^2 \tag{14}$$

Here r_ε is the instantaneous radius of the pore at a specified location across the substrate, and r_o is the initial pore radius. The radius of the deposit is obtained by keeping track of the displacement of the solid-fluid interface, indicated in Eq. 12.

Geometry, Boundary and Initial Conditions

Based on the experiments of Fernandes et al. (Fernandes et al., 2001), the opposed reactant flow geometry (ORFG) is simulated and depicted in Figure 1a. The equations are solved in one dimension. The above set of differential and algebraic Eqs. 1–14 is solved, assuming the following boundary and initial conditions

$$k_{C_i}(C_i^0 - \hat{P}_i C_i) = (j_i^f + j_i^s) \cdot \bar{n}, \text{ at boundary ends} \qquad (15)$$

and

$$C_i = 0, \text{ at } t = 0, \text{ and } i = H_2, P, I \qquad (16)$$

Here k_{c_i} is the external mass-transfer coefficient, P_i is the inverse partition coefficient of species i, C_i^0 is the outside bulk fluid concentration of species i, and $\bar{n}$ is the normal unit vector. In Eq. 15, the external mass flux of species i is equated to the diffusive flux into the substrate. The substrate is initially taken to be free of all species, as indicated by Eq. 16, unless otherwise specified.

Multiscale Strategy

Using the method of lines, the spatial derivatives of Eq. 3 are approximated using a second-order finite difference scheme. The resulting system of differential-algebraic equations is integrated in time using the explicit Euler method at the finest length and time scale, where nucleation and growth occur. The fifth-order, implicit Runge-Kutta solver Radau5 was employed (Hairer and Wanner, 1991) at all other mesh levels (see below for detailed description of mesh levels). During nucleation and growth, sharp spatial gradients exist in the concentration of the intermediate over a relatively small length scale on the order of 0.1 microns. In order to capture atomic-scale features over a 1 mm thick substrate with a uniform mesh, an impracticably large number of O (10^6) nodes is needed. Hence, the adaptive mesh refinement algorithm developed by Berger and Oliger (Berger and Oliger, 1984) is employed to significantly reduce the computation cost and the memory requirements, while being able to resolve phenomena at small scales. This method is often used to solve hyperbolic partial differential equations, and has been successfully used by Choptiuk to solve problems involving critical phenomena in relativity (Choptiuk, 1993).

At the beginning of the process, the numerical solution is relatively smooth because of low nucleation rates. This situation is retained until the concentration of the intermediate builds up to relatively high concentrations (depending on the nucleation rate constant). During this initial period, only one level of refinement, a coarse mesh (l_1) of 101 nodes, is used, as shown in Figure 2. The probability for nucleation at this level is evaluated at each node using Eqs. 9 and 10. In Eq. 10, the volume ΔV_n is assumed to be the volume of a uniform cylinder of radius r_o, and length ΔX_n, where $n = 1$ prior to any nucleation (for the first level) and $n = 4$ after the first nucleation event (for the finest level). As the concentration of the intermediate species increases with time, the probability of nucleation increases. Initial simulations have revealed that, if the probability for nucleation is arbitrarily low, nucleation can start at locations where subsequent growth does not occur. To avoid unnecessary refining of the mesh in such locations, additional constraint is set on the probability for nucleation of the first event to be larger than a threshold value $P_o > P_o^*$. This additional constraint is applied only to minimize the hit-and-miss refinements of the mesh. The selection of P_o^* is described in the results section.

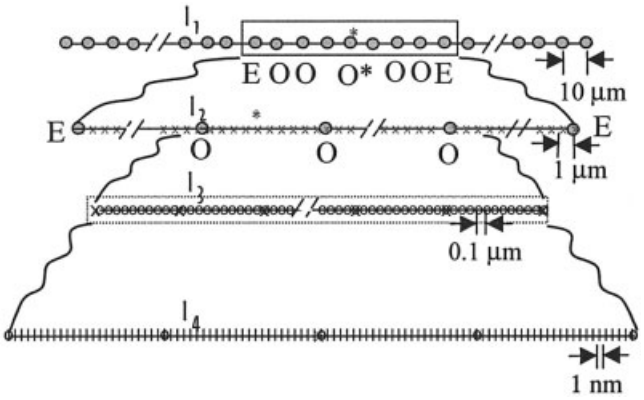

Figure 2. Adaptive mesh refinement used consisting of four levels.

Mesh size of each level is indicated in the figure.

Upon decision for a successful nucleation event on the coarse mesh l_1, a refinement of four nodes on either side of the identified node, indicated by a (*) in Figure 2, is done (9 total nodes, spanning 80 microns of real space) to create the second mesh level. The third and the fourth levels of refinement, are also incorporated at the same time, spanning 40 microns of real space, a width that is adequate for the deposits studied here. A refinement ratio of 10 for the second and third levels, and 100 for the fourth level, are used by successively picking the most probable location at every level. This location is decided by the local concentration (according to Eq. 8), which in turn is computed by cubic spline interpolation from the immediately coarser mesh. For simplicity, once the mesh has been refined, no further changes are done.

The spatial resolution provided by the four levels is adequate to capture nucleation events in space. Due to depletion of the intermediate by nucleation, the subsequent growth of the nuclei, and the opposed flow reactants geometry, the local supersaturation decreases. In addition, the growing deposit decreases the porosity resulting in transport limitations for production of the intermediate, which further lowers the local supersaturation. As a result, nucleation often occurs over short periods of time, and in a spatially limited regime compared to growth. The overall multiscale, hybrid methodology presented here parallels fluid-flow simulations where coarse levels were modeled with continuum fluid mechanics, and fine levels with discrete particle simulations (direct Monte Carlo simulation method) (Garcia et al., 1999).

Communication between mesh levels

The communication between the different levels of refinement is crucial for consistent simulations. For clarity, it is also described between the first and the second levels of refinement. The solution from the first level is used to determine the location in space, indicated by O* in Figure 2, for incorporation

of the second-level mesh based on probability arguments, described previously. The second-level mesh extends four nodes on either side of O*, for numerical robustness. The initial conditions of concentrations for time integration at the second level are obtained by cubic spline interpolation of the concentrations, at time t, corresponding to all nodes E, O, O*, O, and E on l_1. The values at the end nodes E set the boundary values for the second level. The spatial interpolation is done only once for every level, when it is introduced, except for the last level discussed below.

Following upon previous work, the time step for integration at each level l_n is taken to be half of the next coarser level, that is, $\Delta t_n = \Delta t_{n-1}/2$, $n = 2, 3$. Note that this choice controls only the frequency of updating the information between levels, and is much smaller than the diffusion time-scale. With regard to the information passing between scales, the values of the species concentration of the end nodes E on l_2 at t, $t + \Delta t_2$, and $t + 2\Delta t_2$, are obtained from time interpolation of the species concentration, at the corresponding nodes E on l_1 at time t, and $t + \Delta t_1$. Even though the system of differential algebraic equations is integrated implicitly at levels l_1-l_3, with an adaptive time step that is typically very small, compared to the physical time scales, the solution at each level is corrected at predetermined time steps of Δt_n for $n = 1, 2, 3$. For example, at time $t + \Delta t_1$, the solution obtained using the finer mesh l_2 is mapped onto the coarser mesh l_1 at the overlapping nodes O, O*, and O. The same strategy holds for the second and third levels, respectively. The first three levels are used to solve the system of equations describing the conservation of fluid phase species (Eq. 3), whereas the fourth level is dedicated to nucleation and growth. At the fourth refinement level porosity, interfacial surface area, and the consumption of the fluid-phase species by nucleation and growth are determined, and supplied to the coarser levels.

Tracking of the moving interface and evaluation of consumption terms

The nucleus that is seeded onto the finest mesh is assumed to have a height and a depth of 0.5 nm, and a width of 1 nm. The latter dimension is comparable to the resolution of the finest mesh (this is not exactly comparable to the assumption of a critical nucleus of two molecules). A Dirac delta function δ is used to keep track of the nodes where metal deposition can occur. The growth is modeled as a moving interface problem, with the velocity of the interface computed using Eq. 11. When the interface lies between two nodes, the concentration at the interface is obtained by linear interpolation of the two nodes that lie on either side of the interface. The displacement of the interface is obtained by explicit time integration of $dx/dt = V$ using the Euler method. The radial displacement, surface area, and porosity at each node are determined using Eqs. 12–14.

Due to the stochastic nature of nucleation, the average consumption of the intermediate species due to nucleation and growth over an integration time interval Δt_3, is determined by spatial averaging on the finest level l_4, accounting for consumption due to nucleation events, and for growth.

Results and Discussion

Table 1 shows the list of parameters used in the present simulations. Most of the transport parameters and substrate conditions come from the experimental system of Fernandes et al. (2001). The rest of the parameters are not as well known. In particular, the reaction rate constant K_1 is obtained by assuming an activation of 10 kcal/mol, a pre-exponential of 10^{14} cm^3/mol s, and an isothermal system at a temperature of 350 K. K_{Het} is obtained using the rate expression of Hansen and Neurock (2000), with a growth rate constant of 10. A nucleation rate constant of 10^{-6} cm^3/mols is used for the nucleation rate calculation, that is two-orders of magnitude less than that obtained using the collision theory of gases, assuming an activation energy of 45 kcal/mol and a steric factor of 1. The mass-transfer coefficients used in the boundary conditions are obtained from correlations (Cussler, 1997), assuming laminar flow through a circular tube. Using these parameter values as a basis, parametric studies were performed by varying selected parameters from the presented (nominal) values of Table 1.

Table 1. Nominal Values of Simulation Parameters

Reaction Parameters
$K_1 = 10^6$ cm^3/mol s, $K_{\text{Het}} = 10$ (cm^3/mol)$^{0.5}$/s, $K_{\text{Nuc}} = 10^{-6}$ cm^3/mol s
Diffusion Parameters
$D_{m,H_2} = 4 \times 10^{-4}$ cm^2/s, $D_{m,P} = 1.86 \times 10^{-5}$ cm^2/s, $D_{m,I} = 7 \times 10^{-6}$ cm^2/s
$D_{H_2,M} = 10^{-6}$ cm^2/s, $D_{P,M} = D_{I,M} = 0$, $H_{H_2} = 1.0$
Adaptive Mesh Refinement Parameters
$\Delta t_1 = 1 \times 10^{-3}$, $\Delta t_2 = 0.5 \times 10^{-3}$, $\Delta t_3 = 0.25 \times 10^{-3}$, $\Delta t_4 = 0.125 \times 10^{-3}$ (Dimensionless)
$\Delta x_1 = 10^{-3}$, $\Delta x_2 = 10^{-4}$, $\Delta x_3 = 10^{-5}$, $\Delta x_4 = 10^{-7}$ cm
Palladium Properties
$\Omega = 0.1042$ moles/cm^3, $\rho_{\text{Pd}} = 12.2$ g/cm^3
Substrate Properties
$\varepsilon_o = 0.5$, $\tau = 3$, $r_o = 10^{-5}$ cm, $r_{\text{plug}} = 5 \times 10^{-8}$ cm, $L = 1$ mm
Boundary Conditions Parameters
$k_{C_{H2}} = 3 \times 10^{-3}$ cm/s, $k_{C_P} = 6.41 \times 10^{-3}$ cm/s, $k_{C_1} = 1.2 \times 10^{-4}$ cm/s
$\hat{P}_{H_2} = \hat{P}_P = \hat{P}_I = 0.5$
Bulk Fluid Concentrations
$C_P^o = 1.31 \times 10^{-4}$ mol/cm^3, $C_{H2}^o = 6 \times 10^{-6}$ mol/cm^3

The diffusion parameters of H_2 and the precursor, the Pd properties (atomic volume and density), the substrate scales, the external mass transfer coefficients, and the concentrations are estimated for the experimental system of (Fernandes et al., 2001).

First, the role of the threshold in nucleation probability used to refine the mesh at level l_1 is discussed. This threshold is distinctly different from the critical concentration modeled through the Heaviside function in conventional methods. Here, the threshold is used only to identify the potential location for growth in the substrate, and not the nucleation event itself. It is at the finest level that nucleation events can occur based on the nucleation probability. The effect of the threshold probability on the location and time of the first nucleation event is shown in Figure 3. For these simulations, the substrate is initially empty, and the simulation parameters are shown in Table 1. As seen in Figure 3, the lower the threshold probability P_o^*, the lower the time for nucleation. However, premature nuclei do not lead to growth. The dotted line in Figure 3 shows the minimum threshold probability that leads to substantial growth of the deposit. Therefore, for all the simulations presented

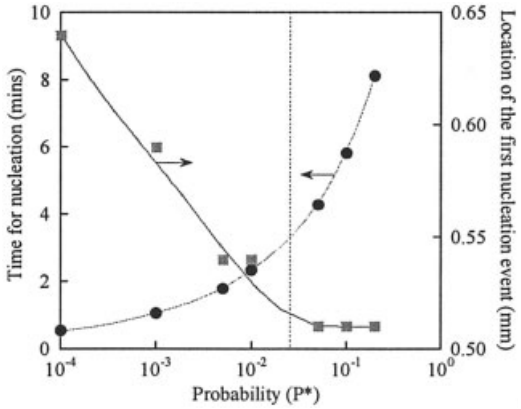

Figure 3. Effect of threshold probability (P_o^*) on the location of the first nucleation event, used for mesh refinement (squares, right vertical axis), and the corresponding time (circles, left vertical axis).

Below a certain threshold, indicated by the dotted line, no growth results in the region where the first nucleation event is chosen. The simulation parameters used are shown in Table 1.

below, P_o^* is set to 0.05, unless otherwise stated. Note that in this and subsequent simulations reported below, the nucleation time and location are stochastic in nature. However, due to the deterministic form of the governing equations at computational levels 1–3, the concentration of the precursor behaves deterministically prior to nucleation. As a result, the choice of the location for mesh refinement at level 1 is unaffected from the value of P_o^*. Small variations in nucleation time and location at level 4 are only observed between independent simulations repeated with different seeds of the random generator. On the average, these changes are much smaller than the changes observed by varying the model parameters discussed below. Thus, only single run simulations (except for Appendix A where multiple runs are carried out) are presented.

Feasibility studies

Figure 4 shows the evolution of the reactants (panel a), intermediate (panel b), and the deposit (panel c), along the length of the substrate, as observed from l_1. Due to higher diffusivity of H_2, the reaction front starts close to the precursor side and moves within the substrate at relatively short times ($t \ll t_1$), which are not shown (t_1 is close to the nucleation time for this case). At longer times ($t > t_1$), the reaction front stabilizes near the stoichiometric location. Assuming quasi-steady state and an infinitely fast reaction R1, it is easy to show (Fernandes et al., 2001) that the stoichiometric location is determined from the ratio of the fluxes of the reacting species, and the stoichiometric coefficients according to reaction R1, and it is equal to $x/L = \mu/(1 + \mu)$, where L is the thickness of the substrate, and $\mu = C_{H_2} D_{m,H_2}/C_P D_{m,P}$ is the ratio of the product of the boundary concentration, and diffusivity of hydrogen to that of the precursor. Given the values of concentrations and diffusivities used here, this location is near the middle of the substrate. While this is an expected result from the quasi-steady-state model, note that simpler transient diffusion-reaction models studied in Gummalla et al. (2003) have shown that this location occurs near the stoichiometric point only when nucleation is relatively slow compared to the species diffusion and the kinetics of intermediate formation (through reaction R1), which is the case for the chosen conditions.

The concentration of the intermediate increases with time, leading to a higher probability for nucleation. After the first nucleation event, the nucleated metal grows autocatalytically in the presence of the intermediate, resulting in the growth of the deposit in both the axial (density dimension) and the lateral direction until the pores are plugged. The profiles of the reactants, intermediate and deposit at short times after nucleation (time t_2), are also shown in Figure 4. The time for pore blocking is arbitrarily defined here as the time taken for plugging a continuous region of the substrate of 100 nm, captured only at levels 3 and 4. At levels l_2 and l_3, the deposit still appears to be growing at a given node, as the concentrations are averaged over larger domains, corresponding to the resolution of these coarser levels. For the current simulation, pore blocking takes place after ~6.5 min. The autocatalytic nature of growth through reaction R3 results in fast depletion of the precursor near the deposition regime. An asymmetry of the intermediate concentration profile resulting from the need for H_2 reduction of the intermediate I is also seen. This asymmetry is also manifested in the deposit itself, as seen from the finest mesh levels in subsequent graphs. At longer times, the intermediate is consumed on the hydrogen side first, and on the precursor side later, as hydrogen starts diffusing through the deposit towards the precursor.

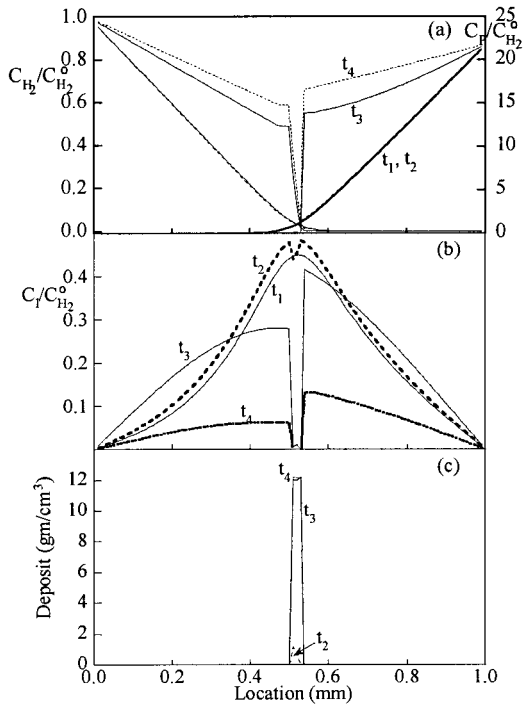

Figure 4. (a) Typical transient profiles of the reactants, (b) intermediate, and (c) the deposit observed from level 1 at times t_1 = 4 min, t_2 = 5.8 min, t_3 = 12 min, and t_4 = 19 min.

The simulation parameters are indicated in Table 1, with P_o^* equal to 0.05.

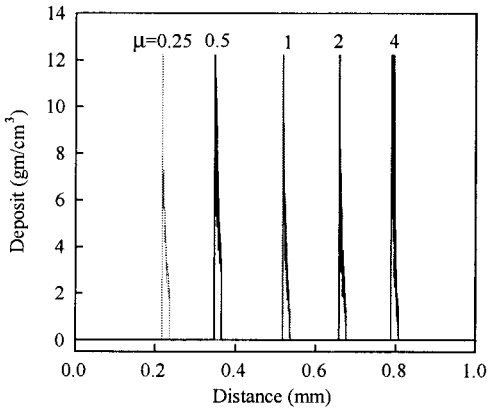

Figure 5. Effect of μ on the location of the deposit as observed from level 4.

The simulation parameters are indicated in Table 1, except for the inlet concentration of C^o_{H2} that varies with μ. $\mu = 1$ corresponds to the nominal case.

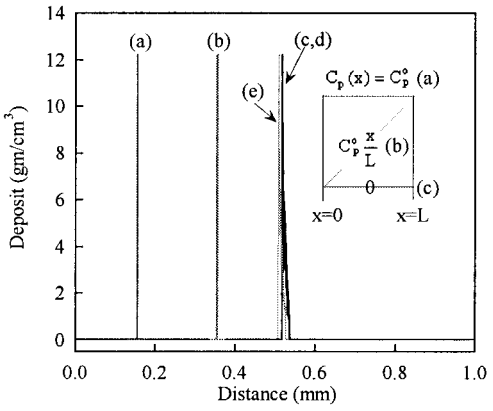

Figure 6. Effect of initial conditions on the location of the deposit for $\mu = 1$.

The simulation parameters used are as indicated in Table 1. (a) Three different initial conditions are considered as depicted in the inset, namely: pores filled with the precursor at the inlet concentration, (b) a linear profile of precursor, and (c) no precursor in the pores. In all cases, hydrogen is not present within the pores at time $t = 0$. Thinner deposits are obtained at pore plugging when the pores are initially filled with precursor. The location of the deposit is considerably shifted towards the hydrogen side with varying initial conditions.

Location of the deposit

As mentioned earlier, in the infinitely fast reaction, quasi-steady-state model of (Fernandes et al., 2001) the location was determined by μ. In order to explore the effect of this dimensionless parameter, Figure 5 shows the profiles of deposit at pore plugging for varying μ, with the remaining conditions as indicated in Table 1. It is seen that μ has a strong effect on the location of the deposit. When μ is less than 1, the deposit is closer to the hydrogen side, as the concentration of hydrogen is higher. Conversely, when μ is greater than 1, the reaction zone is stabilized near the precursor side. The effect of μ on the location of the deposit is in agreement with the simple model (Fernandes et al., 2001), when nucleation is relatively slow compared to diffusion and intermediate formation kinetics.

The transient nature of these simulations along with the importance of the evolutionary nature of deposition found using classic time-dependent, diffusion-reaction models (Gummalla et al., 2003) motivates the exploration of the effect of initial conditions on deposit location. Figure 6 shows the morphology and location of the deposit at pore plugging for three different initial conditions and simulation parameters indicated in Table 1. The initial conditions considered are: (a) pores filled uniformly with the precursor at the inlet concentration; (b) the precursor has diffused into the system to give a linear concentration profile; and (c) no precursor in the pores. These initial conditions are depicted in the inset of Figure 6. In all three cases no hydrogen was initially present in the pores (at time $t = 0$). Very thin deposits are obtained when the precursor is initially present in the substrate pores. In addition, the location of the deposit is considerably shifted towards the hydrogen side, with increasing initial loading of the precursor in the pores. Analysis of the transient species profiles showed that the reaction front starts near the hydrogen side and moves with time into the substrate. For high concentrations, once a nucleus is formed, it grows rapidly to block the pores, resulting in a few nucleation events. In particular, only six nucleation events occurred in case (a) before the pores were plugged. Similar trends, but less dramatic, were observed in case (b). The time for pore plugging was 2 min. and 3.5 min. for cases (a) and (b), respectively. From a practical point of view, the startup of the experiment can be used as another means of controlling the deposit. At the same time, failure to account for the startup could result in apparently nonreproducible results.

Figure 7 compares results from the current multiscale simulations (vertical axis) obtained in Figures 5 and 6, with the simple quasi-steady-state model (horizontal axis) of Fernandes et al. (2001). While the effect of concentration is captured by the quasi-steady-state model, and it is apparent that the effect of the initial conditions on the deposit location is essential. The effect of nucleation-related parameters, namely, the threshold

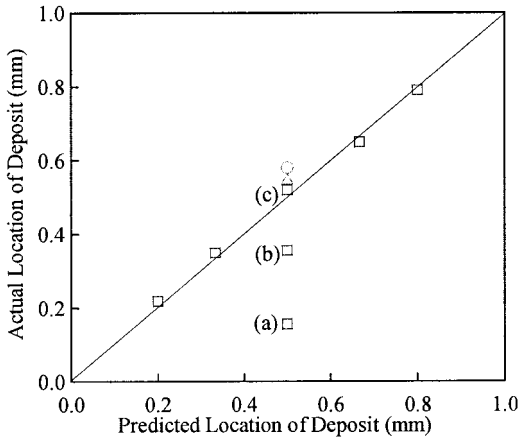

Figure 7. Parity graph showing the location of the deposit as predicted by a simple quasi-steady state model (horizontal axis) and the current multiscale model (vertical axis).

The squares close to the straight line correspond to simulations presented in Fig. 5. Points (a)–(c) correspond to simulations of Figure 6, the triangle to $P^*_o = 0.03$, and the circle to $K_{nuc} = 10^{-5}$ cm^3/mol s. Both μ and the initial conditions have a dominant effect on the location of the deposit.

P_o^*, and the physical parameter K_{nuc} (triangle and circle data points in Figure 7, respectively) have also been studied. The triangle corresponds to parameters indicated in Table 1, with a nucleation threshold of $P_o^* = 0.03$, and the circle to $P_o^* = 0.05$ with an order of magnitude reduction in the nucleation rate constant to $K_{nuc} = 10^{-5}$ cm^3/mols. In these simulations, the location of the deposit is only slightly affected from the nucleation related parameters. Although not studied here, it is expected that faster nucleation and growth may result in a shift of the deposition location towards the precursor side, as has been suggested from simple transient diffusion-reaction models (Gummalla et al., 2003). From Figure 7, it is evident that the location of the deposit is predominantly affected by the initial conditions, and the concentration (and diffusivities, not explicitly shown here) of the reactants, whereas the nucleation kinetics has a minor effect, at least when the latter is slow compared to the processes forming the intermediate.

Growth kinetics

It is expected that the deposit characteristics depend on the relative competition between growth and nucleation. In order to explore this aspect, simulations have been performed by varying the growth rate constant. Figure 8a shows the rate of nucleation dN/dt defined as the fraction of the total nodes of level l_4, which have nucleated per unit time vs. time for three growth rate constants indicated. While the initial nucleation rate is similar in all the three cases (no growth occurs at very short times), nucleation is limited to shorter times for faster growth, due to fast depletion of reactants. Figure 8b shows the effect on deposit thickness and location up to pore plugging as seen from mesh level l_3. It is seen that, for the case of $K_{Het} =$ 1 and 10 (cm^3/mol)$^{0.5}$/s, the location of the deposit is practically unaffected. However, in the case of $K_{Het} = 100$ (cm^3/mol)$^{0.5}$/s the location of pore plugging is shifted by $\sim$ 6 microns toward the precursor side. The pore plugging times calculated for the three cases (with $K_{Het} = 1$, 10, 100 (cm^3/mol)$^{0.5}$/s) are 14 min, 6.5 min, and 5.2 min, respectively, that is, for faster growth, the pores are plugged at shorter times after nucleation.

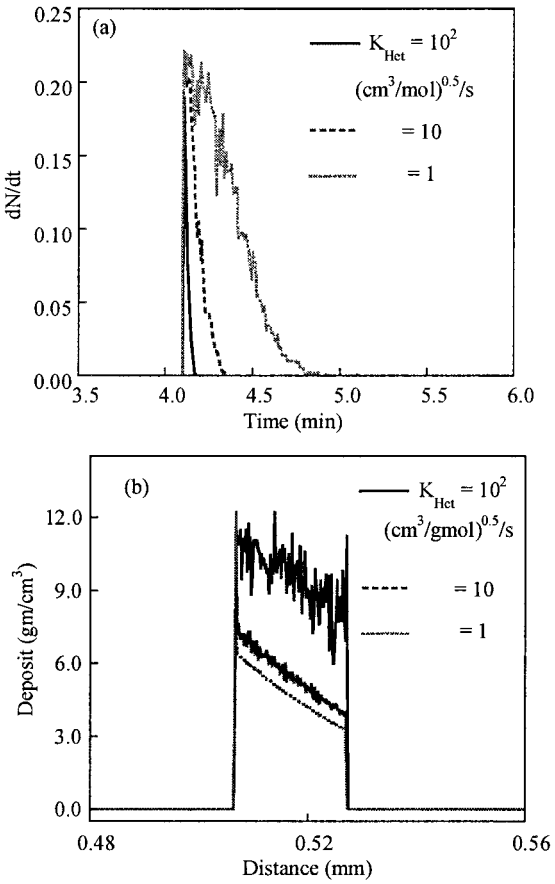

Figure 8. (a) Effect of growth preexponential on the nucleation rate and (b) deposit at pore plugging.

Higher growth rate constants lead to fast growth of nucleated nodes, suppressing further homogeneous nucleation. The total number of nucleated nodes out of 1.5 10^4 of level 4 are 658, 2139, and 6932 for $K_{Het} = 100$, 10, and 1 (cm^3/gmol)$^{0.5}$ s, respectively. Simulation parameters are indicated in Table 1, except for the heterogeneous rate constant indicated in the graph.

For the three cases studied, the morphology of the deposit has also been monitored from the finest level l_4 at the same location in space, and is depicted in Figure 9 for varying times. After pore plugging, the growth rate is controlled by the diffusion of hydrogen through the deposit. This situation results in decreased growth on the precursor side. It takes considerable time after the initial pore plugging to block the pores elsewhere. The most interesting aspect is that the microstructure of the deposit is more uniform at short times, in the case of slow growth rates, because there is enough time for reactants to diffuse around, leading to multiple nucleation events and growth at various special locations. Therefore, film uniformity and defects are affected by the interplay of nucleation and growth kinetics. At long times, the film becomes continuous for all cases.

Evolution of the deposit at longer times

Finally, the evolution of the deposit up to long times, as observed from level l_2, is presented in Figure 10, for simulation parameters indicated in Table 1. Aside from an induction time needed for the first nucleation event, the deposit grows slowly at short times, as the available surface area for growth is low due to the increasing number of nuclei and their initially small size (up to $\sim$5 min). During this time, the concentration of the intermediate builds up, as shown in Figure 4b. With a further increase in time ($\sim$ 6–12 min), the available surface area for growth increases, as shown in Figure 9b, and, hence, there is a rapid depletion of the intermediate on the hydrogen side (see Figure 4b). The reduced concentration of hydrogen on the precursor side leads to a reduction of the growth rate, and, hence, relatively higher concentrations of the intermediate are seen on the precursor side. During the time interval of $\sim$9–15 min, growth is predominantly on the hydrogen side, due to the higher availability of hydrogen. Once the intermediate on the hydrogen side has nearly been depleted, growth occurs mainly on the precursor side, as a consequence of the diffusion of hydrogen through the metal deposit. During this process, any defects in the deposit are "healed," as seen from the deposit morphology at times of 15 min and 25 min. At times greater than 25 min, it is seen that growth is predominantly on the precursor side. From the earlier analysis, it is clear that the

growth at short times is favored on the side of the deposit toward the hydrogen, and at long times toward the precursor.

Conclusions

A multiscale, hybrid computational framework for simulating deposition of films within porous substrates has been developed. The developed model captures the transport of reactants through the pores, homogeneous reaction of the reactants producing an intermediate species, nucleation (treated stochastically), and growth, treated as a moving boundary problem. Adaptive mesh refinement is used to resolve the length scales, varying from nanometer to millimeters. The feasibility of the approach has been demonstrated in the opposed reactant geometry with transport parameters taken from the Pd deposition under supercritical CO_2 conditions.

It has been found that the location and thickness of the deposit within the porous substrate depend strongly on the boundary concentrations and the initial conditions, and, to a lesser extent, on nucleation and growth, at least when these processes are relatively slow. Both boundary concentration and startup details can be used to control deposition, and special attention should be placed on the startup for reproducible results. In addition, it has been shown that the interplay of nucleation and growth kinetics affects the morphology (roughness, defects) of the deposit, and time for pore plugging. The time allowed for growth is important in determining the thickness of the deposit and its roughness.

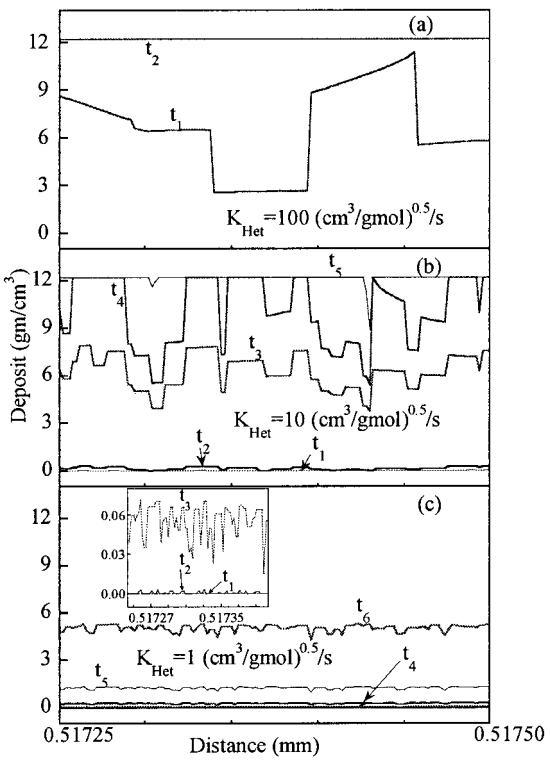

Figure 9. Microstructure of the deposit over a 0.25 μm length at the indicated substrate location, for three different growth rate constants, as seen from level 4.

The transients shown correspond to times $t_{nuc} + t_i$, where $t_1 = 0.5$, $t_2 = 1.2$, $t_3 = 2.5$, $t_4 = 6.3$, $t_5 = 12.5$, and $t_6 = 25$ min, and $t_{nuc} = 4.2$ min. Simulation parameters are indicated in Table 1, except for the varying heterogeneous rate constant.

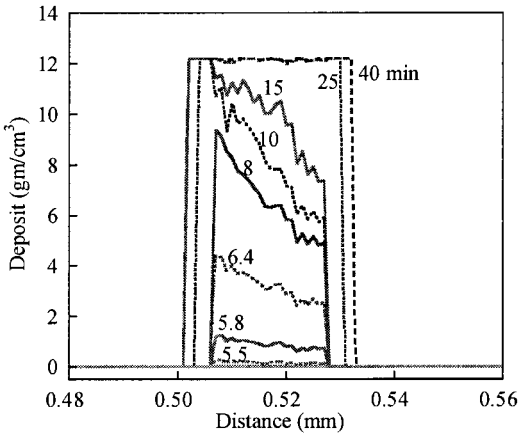

Figure 10. Morphology of the deposit at different times, as observed from level 2 for conditions indicated in Table 1.

Acknowledgments

This work was funded by the National Science Foundation (CTS-9811088).

Literature Cited

Bales, G. S., and D. C. Chrzan, "Dynamics of Irreversible Island Growth during Submonolayer Epitaxy," *Phys. Rev. B,* **50,** 6057 (1994).

Berger, M. J., and J. Oliger, "Adaptive Mesh Refinement for Hyperbolic Partial Differential Equations," *J. Comp. Phys.,* **53,** 484 (1984).

Bhatia, S. K., and D. D. Perlmutter, "A Random Pore Model for Fluid-Solid Reactions: II Diffusion and Transport Effects," *AIChE J.,* **26,** 247 (1980).

Bonilla, G., D. G. Vlachos, and M. Tsapatsis, "Simulations and Experiments on the Growth and Microstructure of Zeolite MFI Films and Membranes Made by Secondary Growth," *Microporous and Mesoporous Materials,* **42,** 191 (2001).

Brune, H., "Microscopic View of Epitaxial Metal Growth: Nucleation and Aggregation," *Surf. Science Reports,* **31,** (1998).

Choptiuk, M. W., "Universality and Scaling in Gravitational Collapse of a Massless Scalar Field," *Phys. Rev. Lett.,* **70,** 9 (1993).

Cussler, E. L., *Diffusion: Mass Transfer in Fluid systems,* Cambridge University Press, New York (1997).

Dee, G. T., "Patterns Produced by Precipitation at a Moving Reaction Front," *Phys. Rev. Letters,* **57,** 275 (1986).

Fernandes, N. E., S. M. Fisher, J. C. Poshusta, D. G. Vlachos, M. Tsapatsis, and J. J. Watkins, "Reactive Deposition of Metal Thin Films Within Porous Supports from Supercritical Fluids," *Chemistry of Materials,* **13,** 2023 (2001).

Fuller, E. N., P. D. Schettle, and J. C. Giddingd, "A New Method for Prediction of Binary Gas-Phase Diffusion Coefficients," *Ind. and Eng. Chemistry,* **58,** 19 (1966).

Garcia, A. L., J. B. Bell, W. Y. Crutchfield and B. J. Alder, "Adaptive Mesh and Algorithm Refinement Using Direct Simulation Monte Carlo," *J. Comp. Phys.,* **154,** 134 (1999).

Gavalas, G. R., "A Random Capillary Model with Application to Char Gasification at Chemically Controlled Rates," *AIChE J.,* **26,** 577 (1980).

Gillespie, D. T., "A General Method for Numerically Simulating the Stochastic Evolution of Coupled Chemical Reactions," *J. Comp. Phys.,* **22,** 403 (1976).

Gillespie, D. T., "Exact Stochastic Simulation of Coupled Chemical Reactions," *J. Phys. Chem.,* **81,** 2340 (1977).

Gilmer, G., "Computer Models of Crystal Growth," *Science,* **208,** 355 (1980).

Girshick, S. L., M. T. Swihart, S.-M. Suh, M. R. Mahajan, and S. Nijhwan, "Numerical Modeling of Gas-Phase Nucleation and Particle Growth During Chemical Vapor Deposition of Silicon," *J. Electrochem. Soc.,* **147,** 2303 (2000).

Gummalla, M. "Transport-Chemistry Coupling in Cocurrent and Countercurrent Flow Configurations: Applications to Nonlinear Dynamics of Flames and Deposition of Membranes in Porous Media." PhD Thesis, Dept. of Chemical Engineering. University of Massachusetts, Amherst (2002).

Gummalla, M., M. Tsapatsis, J. J. Watkins, and D. G. Vlachos, "The Roles of Transients and Nucleation in Film Deposition within a Support," *Ind. Eng. Chem. Res.,* **42,** 1321 (2003).

Gyure, M. F., C. Ratsch, B. Merriman, R. E., Caflisch, S. Osher, J. J. Zinck, and D. D. Vvedensky, "Level-Set Methods for the Simulation of Epitaxial Phenomena," *Phys. Rev. E,* **58,** 6927 (1998).

Hairer, E., and G. Wanner, *Solving Ordinary Differential Equations II. Stiff and Differential Algebraic Problems,* Springer-Verlag, Berlin (1991).

Hansen, E. W., and M. Neurock, "First-Principles-Based Monte Carlo Simulation of Ethylene Hydrogenation Kinetics on Pd.," *J. Catal.,* **196,** 241 (2000).

Hashimoto, K., and P. L. Silveston, "Gasification: Part I. Isothermal Kinetic Control Model for a Solid with a Pore Distribution," *AIChE J.,* **19,** 259 (1973).

Hill, C. G., *An Introduction to Chemical Engineering Kinetics and Reaction Engineering,* Wiley, New York (1977).

Hongqin, L., and E. Ruckenstein, "Predicting the Diffusion Coefficients in Supercritical Fluids," *Ind. Eng. Chem. Res.,* **36,** 888 (1997).

Katsoulakis, M., A. J. Majda, and D. G. Vlachos, "Coarse-Grained Stochastic Processes for Microscopic Lattice Systems," *Proc. Natl. Acad. Sci.,* **100,** 782 (2003).

Kerkhof, P., "A modified Maxwell-Stefan Model for Transport Through Inert Membranes: The Binary Friction Model," *Chem. Eng. J.,* **64,** 319 (1996).

Kerkhof, P., "On the Isothermal Binary Mass Transport in a Single Pore," *Chem. Eng. J.,* **83,** 107 (2001).

Kirchheim, R., T. Mutschelle, W. Kieninger, H. Gleiter, R. Birringer, and T. D. Koble, "Hydrogen in Amorphous and Nanocrystalline Metals," *Mater. Sci. Eng.,* **99,** 457 (1988).

Kyu, T., and H.-W. Chiu, "Spatiotemporal Growth of Faceted and Curved Single Crystals," *Phys. Rev. E,* **61,** 4161 (2002).

Lam, R., T. Basak, D. G. Vlachos, and M. A. Katsoulakis, "Validation of Mesoscopic Theories and their Application to Computing Effective Diffusivities," *J. Chem. Phys.,* **115,** 11278 (2001).

Lam, R., and D. G. Vlachos, "A Multiscale Model for Epitaxial Growth of Films: Growth Mode Transition," *Phys. Rev. B,* **64,** 5401 (2001).

Lebedeva, M. I., D. G. Vlachos, and M. Tsapatsis, "Bifurcation Analysis of Liesegang Ring Pattern Formation," *Phy. Rev. Lett.*, in press (2004).

Lin, Y. S., and A. J. Burggraaf, "Modeling and Analysis of CVD Process in Porous Media for Ceramic Composite Fabrication," *Chem. Eng. Sci.,* **46,** 3067 (1991).

Mason, E. A., and A. P. Malinauskas, *Gas transport in porous media: The Dusty Gas Model,* Elsevier, Amsterdam (1983).

Novak, M., K. Ehrhardt, K. Klusacek, and P. Schneider, "Dynamics of Non-Isobaric Diffusion in Porous Catalysts," *Chem. Eng. Sci.,* **43,** 185 (1988).

Ofori, J. Y., and S. V. Sotirchos, "Multicomponent Mass-Transport in Chemical-Vapor Infiltration," *Ind. Eng. Chem. Res.,* **35,** 1275 (1996).

Osher, S., and J. A. Sethian, "Fronts Propagating with Curvature Dependent Speed: Algorithms Based on Hamilton-Jacobi Formulations," *J. Comp. Phys.,* **79,** 12 (1988).

Raimondeau, S., and D. G. Vlachos, "Recent Developments on Multiscale, Hierarchical Modeling of Chemical Reactors," *Chem. Eng. J.,* **90,** 3 (2002).

Ratsch, C., M. F. Gyure, S. Chen, M. Kang, and D. D. Vvedensky, "Fluctuations and Scaling in Aggregation Phenomena," *Phys. Rev. B,* **61,** 598 (2000).

Reid, R. C., J. M. Prausnitz, and B. E. Poling, *Properties of gases and liquids,* McGraw-Hill, New York (1987).

Sahimi, M., G. R. Gavalas, and T. T. Tsotsis, "Statistical and Continuum Models of Fluid-Solid Reactions in Porous Media," *Chem. Eng. Sci.,* **45,** 1443 (1990).

Samseth, J., M. B. Kirkedelen, F. A. Maao, A. Hansen, and M.-A. Einarsrud, "Liesegang Pattern Formation by Gas Diffusion in Silica Aerogels," *J. Non-Crystalline Solids,* **225,** 298 (1998).

Scappin, M., and P. Canu, "Analysis of Reaction Mechanisms Through Stochastic Simulation," *Chem. Eng. Sci.,* **56,** 5157 (2001).

Simons, G. A., and M. L. Finson, "Structure of Coal Char I: Pore Branching," *Combust. Sci. Technol.,* **19,** 217 (1979).

Sloot, H. J., C. A. Smolders, W. P. M. van Swaiij, and G. F. Versteeg, "High Temperature Membrane Reactor for Catalytic Gas-Solid Reactions," *AIChE J.,* **38,** 887 (1992).

Snyder, M. A., D. G. Vlachos, and M. A. Katsoulakis, "Mesoscopic Modeling of Transport and Reaction in Microporous Crystalline Membranes," *Chem. Eng. Sci.,* **58,** 895 (2003).

Sotirchos, S. V., and S. Zarkanitis, "A distributed Pore Size and Length Model for Porous Media Reacting with Diminishing Porosity," *Chem. Eng. Sci.,* **48,** 1487 (1993).

Szekely, J., and J. W. Evans, "A Structural Model for Gas-Solid Reactions with a Moving Boundary," *Chem. Eng. Sci.,* **25,** 1091 (1970).

Toschev, S., A. Milchev, and S. Stoyanov, "On Some Probabilistic Aspects of the Nucleation Process," *J. Cryst. Growth,* **13/14,** 123 (1972).

Troiano, A. R. *Hydrogen in Metals. Proc. of an Int. Conf. on the Effects of Hydrogen on Materials Properties and Selection and Structural Design,* Champion Press, Philadelphia, PA (1973).

Tsapatsis, M., and G. Gavalas, "Modeling of SiO_2 Deposition in Porous Vycor: Effects of Pore Network Connectivity," *AIChE J.,* **43,** 1849 (1997).

Tsapatsis, M., and G. R. Gavalas, "A kinetic Model of Membrane Formation by CVD of SiO_2 and Al_2O_3," *AIChE J.,* **38,** 847 (1992).

Vekilov, P. G., H. Lin, and F. Rosenberger, "Unsteady Crystal Growth due to Step-Bunch Cascading," *Phys. Rev. E,* **55,** 3202 (1997).

Vlachos, D. G., and M. A. Katsoulakis, "Derivation and Validation of Mesoscopic Theories for Diffusion of Interacting Molecules," *Phys. Rev. Letters,* **85,** 3898 (2000).

Ward, T. L., and T. Dao, "Model of Hydrogen Permeation Behavior in Palladium Membranes," *J. of Mem. Sci.,* **153,** 211 (1999).

Xomeritakis, G., and Y. S. Lin, "Chemical Vapor Deposition of Solid Oxides in Porous Media for Ceramic Membrane Preparation. Comparison of Experimental Results with Semianalytical Solutions," *Ind. Eng. Chem. Res.,* **33,** 2607 (1994a).

Xomeritakis, G., and Y. S. Lin, "CVD of Solid Oxides in Porous Media for Ceramic Membrane Preparation or Modification. Explicit Solutions for Deposition Characteristics," *Chem. Eng. Sci.,* **49,** 3909 (1994b).

Xomeritakis, G., and Y. S. Lin, "CVD Synthesis of Gas Permeation Properties of Thin Palladium/Alumina Membranes," *AIChE J.,* **44,** 174 (1998).

Appendix: Testing of the Hybrid Simulation Approach

Here the validity of the proposed hybrid approach is assessed with simple, well-mixed 1 nm^3 reactor simulations (scale appropriate for nucleation). This reactor can be thought of as one-node of the full model. Transport of reagents is ignored, but possible changes in the concentration of the intermediate are induced in an ad-hoc manner, described below. Two parallel reactions are considered, namely, generation of the precursor for nucleation, I, from reactants H_2 and P, through reaction R1, and generation of the nucleus M from the intermediate I, according to reaction R2. Here, $k_2 \ll k_1$ is assumed to represent a rare nucleation event, where k_2 and k_1 denote the rate constants for the nucleation, and the dominant reaction, respectively.

In the first case, the analytical expression for computing the temporal probability (Eq. 9) is verified by comparing it to Monte Carlo (MC) simulations for constant (time-independent) concentrations of all reagents. For this purpose, a fixed number of 100 molecules of H_2, P, and I each are considered. When the concentrations of H_2, P, and I are fixed and equal, the probability for nucleation at a given instant is $r = k_2/(k_1 + k_2)$, and the rate of nucleation is given by Eq. 10. Kinetic MC simulations have been performed following Gillespie's algorithm (Gillespie, 1976, 1977), without changing the number of

H_2, P, and I molecules. The probability computed using MC simulations for having at least one successful nucleation event after elapsed time t, denoted as $P_{>=1}$, is shown with lines in Figure A1 for different values of r. The results have been obtained from $\sim 10^5$ independent simulations. The circles are obtained from Eq. 9, with $\Delta t = 1$. The excellent agreement between the two methods is not surprising given the constant concentrations in the system. The physics in this case is captured exactly by the Poisson distribution used in the hybrid approach.

In the second case, the validity of the hybrid approach was tested, when the concentration of the intermediate changes with time, a situation that mimics the actual deposition system better. These calculations were performed with a constant number of 50 molecules of H_2 and 50 molecules of P. The reactor is assumed to be initially empty of the intermediate I. The concentration of I builds up with time through reaction R1, with constant rate r_1. In the fully stochastic MC simulations, two bimolecular events can happen, namely the formation of I, with a rate r_1, and the formation of nucleus M, with a rate r_2. The probability for picking a nucleation event is $r = r_2/(r_1 + r_2)$. At each instant, the transition probabilities per unit time are computed, the time is advanced, and an event is picked. At short times, reaction R1 is picked, and the number of I molecules increases. Once the concentration of I has increased, a nucleation event happens. The time for the first nucleation event is recorded, and thus, the simulation is repeated to obtain the probability density function. The results have been obtained from $\sim 10^5$ independent simulations to ensure the asymptotic (converged) behavior.

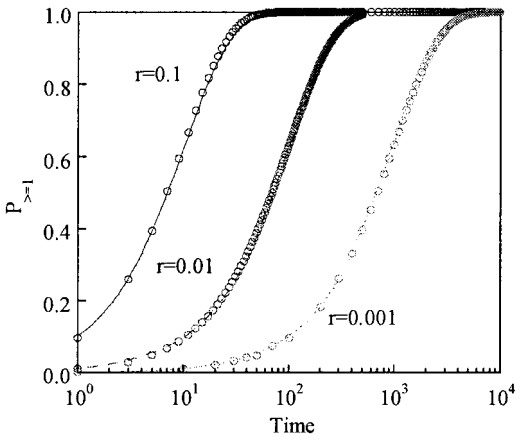

Figure A1. Comparison of 10^5 independent Monte Carlo simulations with analytical expression (Eq. 9) for three constant values of r indicated.

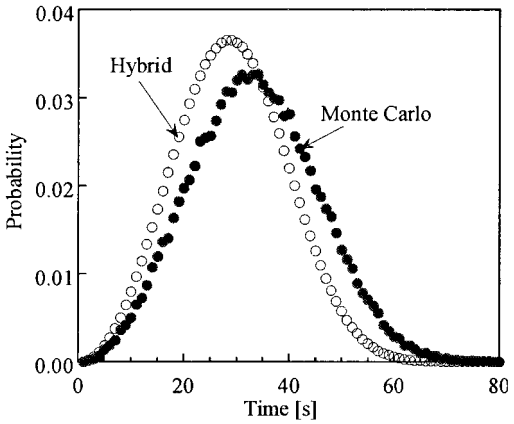

Figure A2. Comparison of probability density function obtained from 10^5 fully stochastic, independent Monte Carlo simulations (filled circles) and hybrid simulations (Eqs. 9, 10, and A1) shown as open symbols for $k_1 = 0.1$ and $k_2 = 10^{-5}$ nm^3/mol s.

The rest of the parameters are given in the text.

For the hybrid simulations, the concentration of I increases according to

$$dC_I/dt = r_1 \tag{A1}$$

which is solved using the explicit Euler method. At each time step, the rate of nucleation is computed using Eq. 10, and the probability of nucleation is computed using Eq. 9, and is compared with the random number to determine whether a nucleation event would occur. With increasing time, the probability for nucleation increases until a successful nucleation event occurs.

The comparison of the probability density function for nucleation is obtained from the hybrid approach, and the fully stochastic MC simulation is shown in Figure A2, for the rate constants indicated. Additional runs were performed for other combinations of parameters, similar to those shown in Figure A1. Reasonable agreement is found in all the cases studied, even with widely varying rate constants. The differences between MC and the hybrid approach are attributed to the time varying concentration of the intermediate I, as the Poisson distribution is only exact for a constant supersaturation (Toschev et al., 1972).

Manuscript received Jan. 7, 2003, and revision received July 3, 2003.